Journal of Power Sources 269 (2014) 509–519

Contents lists available at ScienceDirect

Journal of Power Sources

journal homepage: www.elsevier.com/locate/jpowsour

$LaNi_{0.6}Co_{0.4}O_{3-\delta}$ dip-coated on Fe–Cr mesh as a composite cathode contact material on intermediate solid oxide fuel cells

Aroa Morán-Ruiz [a], Karmele Vidal [a], Aitor Larrañaga [a, *], Miguel Angel Laguna-Bercero [b], Jose Manuel Porras-Vázquez [c], Peter Raymond Slater [c], María Isabel Arriortua [a, *]

[a] Universidad del País Vasco (UPV/EHU), Facultad de Ciencia y Tecnología, Departamento de Mineralogía y Petrología, Barrio Sarriena S/N, 48940 Leioa, Vizcaya, Spain
[b] CSIC-Universidad de Zaragoza, Instituto de Ciencia de Materiales de Aragón (ICMA), Pedro Cerbuna 12, 50009 Zaragoza, Spain
[c] University of Birmingham, School of Chemistry, Birmingham B15 2TT, UK

HIGHLIGHTS

- After 1000 h at 800 °C LNC/Fe–Cr mesh still present adequate mechanical integrity.
- ASR value for LNC/Fe–Cr mesh with interconnect was 5.40 ± 0.01 mΩ cm^2 at 800 °C.
- Cr deposition under the channel is higher than under the rib of the interconnect.

ARTICLE INFO

Article history:
Received 24 March 2014
Received in revised form
13 June 2014
Accepted 7 July 2014
Available online 15 July 2014

Keywords:
IT-SOFC
Composite contact material
Channeled interconnect
Ohmic resistance losses
Electrical contact
$LaNi_{0.6}Co_{0.4}O_{3-\delta}$

ABSTRACT

The feasibility of using Crofer22APU mesh dip coated with $LaNi_{0.6}Co_{0.4}O_{3-\delta}$ (LNC) ceramic paste as a uniform contact layer on a Crofer22APU channeled interconnect was studied. The control of LNC dip coating thickness on Fe–Cr mesh was carried out by rheological measurements of the suspension. SEM cross-section of formed composite contact material showed good adherence between ceramic and metallic components. The measured area specific resistance (ASR) value at 800 °C was 0.46 ± 0.01 mΩ cm^2, indicating low contact resistance itself. The long term stability of metallic/ceramic composite was also studied. The contact resistance, when composite contact material was adhered to channeled Crofer22APU interconnect, was 5.40 ± 0.01 mΩ cm^2, which is a suitable value for the performance of IT-SOFC stack. The stability of the system after treating at 800 °C for 1000 h was characterized using X-ray Micro-Diffraction (XRMD), Scanning Electron Microscope equipped with an Energy Dispersive X-ray analyzer (SEM-EDX) and X-ray Photoelectron Spectroscopy (XPS) techniques. The oxidation rate of the alloy and Fe_3O_4 phase formation were enhanced on the channels of the interconnect. Thus, the formation of CrO_3 (g) and $CrO_2(OH)_2$ (g) species was accelerated on the composite surface under the channel. Through XRMD and XPS analysis the coexistence of two perovskite phases (initial LNC and Cr-perovskite) was observed.

1. Introduction

Global warming and its detrimental climatological, ecological and sociological effects have led to an increasing interest in more efficient and clean power systems [1]. High temperature solid oxide fuel cells (HT-SOFCs, operating in the range of 800–1000 °C) have a good potential for being used as stationary stand-alone power generation systems [2]. For these applications, chemical to electrical efficiency of HT-SOFC is in the range of 45–65% [3]. For smaller scale applications, such as micro combined heat and power (micro-CHP), small auxiliary power units (APUs) and small electrical generators [4], there is a need to lower operation temperatures, into the intermediate temperatures (IT) range of 500–800 °C. Lower temperature operation affords more rapid start-up and shutdown.

A single SOFC cell produces ~0.6–0.7 V under normal working conditions [3]. Therefore, in order to obtain the desired electric power output, single cells are connected and fabricated together to form a stack using interconnect and sealing materials [5]. In HT-

* Corresponding authors. Tel.: +34 946015984; fax: +34 946013500.
E-mail addresses: aitor.larranaga@ehu.es (A. Larrañaga), maribel.arriortua@ehu.es (M.I. Arriortua).

http://dx.doi.org/10.1016/j.jpowsour.2014.07.040
0378-7753/

SOFCs, the bond between the cell and the $LaCrO_3$ interconnect is typically realized by sintering at 1300 °C. A solid bond with good electrical contact is obtained and no other contact material is then required. However, for IT-SOFC chromium-containing ferritic stainless steels are generally used as interconnect [6,7] and, contact materials are needed to provide a homogeneous bonding between interconnect and electrode to avoid power losses [8]. Previous studies [9,10], based on the effect of contact between electrode and current collector on the performance of SOFCs, concluded that when the contact area of the current collector increased from 4.6% to 27.2%, the cell resistance decreased from 1.43 to 0.19 Ω cm^2 at 800 °C.

The oxide scale formed on the surface of Fe–Cr alloys, after long exposure in the SOFC environment, results in volatile chromium (Cr) species such as CrO_3 and $Cr_2(OH)_2$ (in presence of vapor) [3]. These species can cause rapid performance deterioration in SOFCs due to the deposition of Cr at the bulk electrode and at the electrolyte/electrode interface regions [11]. The cathode contact materials can act as a barrier to the migration of chromium from the metallic to the cathode and further minimize the area specific resistance (ASR) between both materials [12–14].

The cathode contact materials compositions should fulfill the following requirements [15,16]: i) high electrical conductivity and appropriate sintering activity to minimize the resistance of the contact layer itself and to protect the steel substrate from excessive oxidation, ii) chemically compatible and appropriate thermal expansion behavior with adjacent materials and, iii) high thermochemical and structural stability in the oxidizing cathode environment. The materials used as contact layers include: i) noble metals (Ag) or noble metal-perovskite composites (Ag-$(La_{0.6}Sr_{0.4})(Co_{0.8}Fe_{0.2})O_3$, Ag–$La_{0.8}Sr_{0.2}MnO_3$), ii) conventional perovskite cathode materials (such as, $La_{0.6}Sr_{0.4}Co_{0.2}Fe_{0.8}O_3$, $La_{0.8}Sr_{0.2}FeO_3$), iii) oxides with a spinel structure, M_3O_4 (M = Ni, Mn, Co, Cu, Fe), or iv) recently developed oxides like $Ni_{0.33}Co_{0.67}O$. Despite the interactions of these kind of materials which formed oxide scale on metal surface, due to their susceptibility to form phases like Ag_2CrO_4, $AgCrO_2$, $SrCrO_4$, Cr-spinels or Cr-perovskites, the use of those materials, in most cases, are quite effective for improving the electrical contact between the cathodes and metallic interconnects [17–25]. In addition, these materials can reduce the oxidation rate of the steel and minimize the formation of new phases arising from the oxidation of metal itself such as, Fe_2O_3 and Fe_3O_4 [26]. In this study, $LaNi_{0.6}Co_{0.4}O_{3-\delta}$ (LNC) ceramic composition was selected, due to the adequate sintering activity, electrical conductivity and thermal expansion coefficient (TEC) [17], coupled with ferritic stainless steel Crofer22APU mesh to form a ceramic/metallic composite contact material. Crofer22APU was developed to increase the electrical conductivity of the scale and to reduce the chromium vaporization. This is achieved by adding 0.5% Mn in its composition which facilities the $(Cr,Mn)_3O_4$ spinel formation [3]. The use of a high conductivity perovskite type material in conjunction with stainless steel mesh is expected to improve current collection. At the same time, it achieves a continuous contact on the ribs without sacrificing the flow of the air through the channels. Taking into account our previous studies [17,27] the use of this composite material between Crofer22APU interconnect and $La_{0.6}Sr_{0.4}FeO_3$ cathode in flow channel configuration, can offer an adequate mechanical integrity and low reactivity between the applied layers without compromising the contact resistance of the system.

The goal of this work is to develop a metallic/ceramic composite contact material achieving a good bonding between this contact material and the channeled metallic interconnect. An adequate formulation of the LNC ceramic slurry was set and then dip coated [28,29] on Crofer22APU mesh. The electrical resistance, chemical compatibility and adherence between ceramic and metallic parts of the composite material, under long term IT-SOFC operating conditions, were determined. Results of electrical performance of the contact material/interconnect system are presented. In addition, long term contact stability of the metallic/ceramic composite material under the rib (direct contact) and channel (indirect contact) of the interconnect was analyzed.

In order to understand the interactions between the Crofer22-APU alloy and the LNC ceramic material the following issues were considered [3,30]: i) the preoxidized alloys form protective and semi-conductive chromia oxide and a dense and stable $(Cr,Mn)_3O_4$ spinel on the surface of the alloy, which is effective to reduce the generation of volatile Cr species ii) the reason for the Cr volatility is the thermodynamic instability of chromia scales formed on the alloy, forming gaseous species (CrO_x (x = 1,2,3)); and iii) the deposition process of Cr species at the ceramic coating, under SOFC operation conditions, can be described by the nucleation deposition theory.

2. Experimental

The formulation of ceramic powder used in this study was $LaNi_{0.6}Co_{0.4}O_{3-\delta}$ (LNC) (NexTech, Fuel Cell Materials). To obtain metallic/ceramic contact composite, Crofer22APU stainless steel mesh (Fiaxell SOFC Technologies), with mesh opening of about 175 μm and a thickness of 250 μm, was cut into 10 × 10 mm squares, cleaned with acetone in an ultrasonic bath and dried. The squared-meshes squares were preoxidized at 600 °C for 10 h and then dip coated with an LNC ceramic paste (dip coating rate = 4.5 mm s^{-1}). The chemical composition of the steel, as given by the supplier, is listed in Table 1. The ceramic slurry was composed of ceramic powder (LNC), dispersant (Dolapix, Zschimmer & Schwarz, Chemische Fabriken), binder (PVB, polyvinyl butyral, Solutia Solutions) and solvent (ethanol, Panreac). The paste composition was based on the formulation shown in Table 2. Particle size distribution of the ceramic powder was carried out using a Mastersizer particle size analyzer (Malvern Instruments). Rheology of the suspensions was analyzed using a rheometer (HAAKE MARS II) at shear rates from 0.1 s^{-1} to 1000 s^{-1}, and at room temperature. Ceramic/metallic material was sintered at 1050 °C for 2 h [9] and then treated at 800 °C for 1000 h, in open air.

The composite contact material was bonded to a Crofer22APU channeled interconnect (ThyssenKrupp VDM). The channels of substrate are 2 mm width, 0.5 mm depth, 10 mm length and the distance between neighboring is 2 mm (Fig. 1). The substrate was cut into 10 × 10 mm and 1 mm thick pieces, polished using #800 grit SiC paper and then, cleaned with acetone in an ultrasonic bath and dried. Subsequently, they were preoxidized at 800 °C for 100 h. An additional layer of LNC was coated on the ribs of the interconnect substrate by colloidal spray technique [31]. The composite contact material was directly adhered to the interconnect, sintered at 1050 °C for 2 h and then treated at 800 °C for 1000 h. The reactivity between the contact material and the rib and channel of the Fe–Cr interconnect, after long term heated at 800 °C in open air, was characterized according to the scheme shown in Fig. 1. All the experiments were performed in open air so the moisture level in the incoming air stream can be establish considering that the water vapor (H_2O) in air is around 0.001–5% by volume. However, these

Table 1
Composition of the Crofer22APU steel in wt%.

	Cr	Fe	Mn	Ti	Si	Al	La	Others
Crofer22APU	22	Bal.[a]	0.5	0.1	0.25	0.25	0.15	0.28

[a] Balance.

Table 2
Ceramic slurry composition prepared for dip-coating.

Ceramic slurry composition	Volume %
Ceramic powder, LNC	12.5
EtOH	87.5
Dispersant, Dolapix	1% regarding to the ceramic powder
Binder, PVB	5% regarding to the ceramic powder

values depend on the temperature so it was difficult to determine a moisture numerical value in the performed experiments. Nevertheless, in order to analyze Cr species formation over the chromium scale it has been considered a wet atmosphere.

X-ray Micro-Diffraction (XRMD) data were collected using a Bruker D8 Discover diffractometer equipped with a Cu Twist tube, Ni filter (λ = 1.5418 Å), PolyCap™ (1μ single crystal cylinders) system for parallel been generation (divergence of 0.25°), and a 1-D LynxEye PSD detector (active length in 2θ 2.7°). The sample was mounted on an Eulerian Cradle with automatic controlled X–Y–Z stage. The sample illumination was adjusted with 1 mm PinHole collimator in the incident beam, the position control was tested by using the interference of two lasers. Data were collected from 10 to 100° 2θ (step size = 0.04 and time per step = 10 s total time 6.5 h) at RT.

Surface and cross-section of the samples were analyzed by a scanning electron microscope (SEM, JEOL LSM-6400) equipped with an Oxford Pentafet energy dispersive X-ray analyzer (EDX). Secondary electron images (SE) were taken at 20 kV and $1.1 \cdot 10^{-11}$ A using a working distance of 7 mm. Composition analysis was performed using back-scattered electrons (BSE) at 20 kV accelerating voltage, $1 \cdot 10^{-9}$ A current density and 15 mm working distance. For the cross-section analysis, samples were embedded in epoxy resin, polished using standard metallographic techniques, and coated with a coal graphite layer (10 nm) that was deposited by evaporation (BLA-TEC SCD 004 Sputter Coater) to provide electrical conductivity. INCA 350 software (Oxford Instrument) was used to reconstruct the spectra, and Fe, Cr, Mn and an LNC pellet were used as standards.

X-ray photoelectron spectroscopy (XPS) measurements were carried out in an SPECS (Berlin, Germany) system equipped with a Phoibos 150 1D-DLD analyzer and monochromatic Al K_α radiation (1486.6 eV). The analysis of the present elements were made at wide scan mode (step energy 1 eV, dwell time 0.1 s, pass energy 80 eV) and after that, high-resolution spectra of the found elements were acquired (step energy 0.1 eV, dwell time 0.1 s, pass energy 20 eV) with an electron take-off angle of 90°. The binding energies were calibrated using C1s peak (BE = 284.6 eV) as an internal standard.

Area Specific Resistance (ASR) measurements were performed using the DC four-probe method (the resistance value was estimated from the voltage value (c 1604 Digital Multimeter) measured on applying a current of 1A (Thurlby Thandar Instruments PL300 current source) [32], on both LNC dip-coated Crofer22APU mesh composite (Fig. 2a) and on a system, which was prepared according to the geometries shown in Fig. 2b, in open air. Electrical contacts between samples and external measuring circuit were made using two Pt wires directly welded onto the sides of the interconnect, and using Pt paste and Pt mesh onto the surface of the composite contact material.

3. Results and discussion

3.1. Control of LNC dip coating thickness on Fe–Cr mesh

Prior to the rheological characterization, particle size distribution measurements were performed on LNC powders, since this parameter influences the rheological properties. Fig. 3 shows a monomodal size distribution of LNC powder (d_{50}: 2.37 μm). The characterization of LNC slurries by rheological measurements is important to control coated thicknesses during the dip coating process. A summary of the composition of the slurry is shown in Table 2. Rheological characterization of the suspensions showed a newtonian fluid behavior, which means that the viscosity values are independent of the shear rate. Typical viscosity values are in the range of 0.054 Pa s, leading to a LNC thickness of the layers after dip-coating and sintering of ~500 μm.

3.2. Characterization of composite contact material

LNC ceramic slurries were dip coated on preoxidized Crofer22-APU stainless steel mesh and sintered at 1050 °C for 2 h in order to form the composite contact material. Fig. 4 shows surface morphology SEM micrographs of Fe–Cr mesh before and after sintering the LNC layers. The area specific resistance (ASR) value of the metallic/ceramic composite material was 0.46 ± 0.01 mΩ cm^2 at 800 °C. This minimal ASR value confirms that the use of this composite material as a contact layer is adequate. SEM cross-section (Fig. 5) of the obtained ceramic-metallic composite contact material, after ASR measurements, showed good adherence between LNC ceramic material and Crofer22APU mesh, due to similar TEC values between Crofer22APU and LNC materials [17]. As observed from Fig. 5, the ceramic coating is continuous and homogenous along the sample.

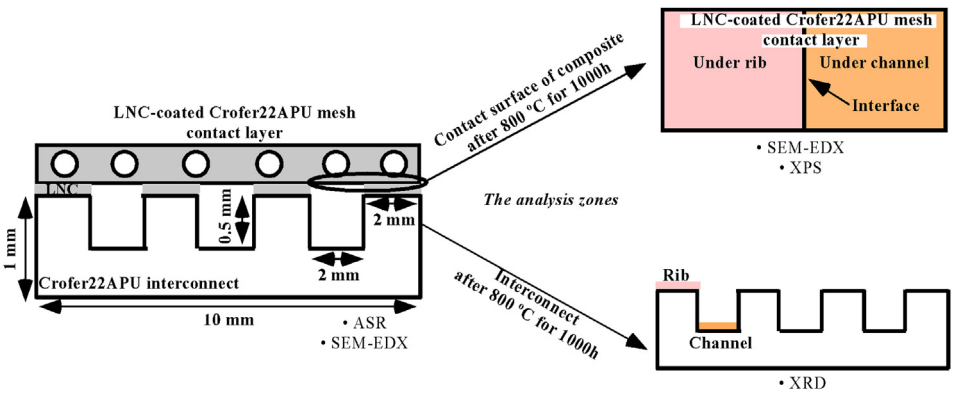

Fig. 1. Schematic representation of the characterization of {LNC dip-coated on Crofer22APU mesh composite contact material/Crofer22APU channeled interconnect} system.

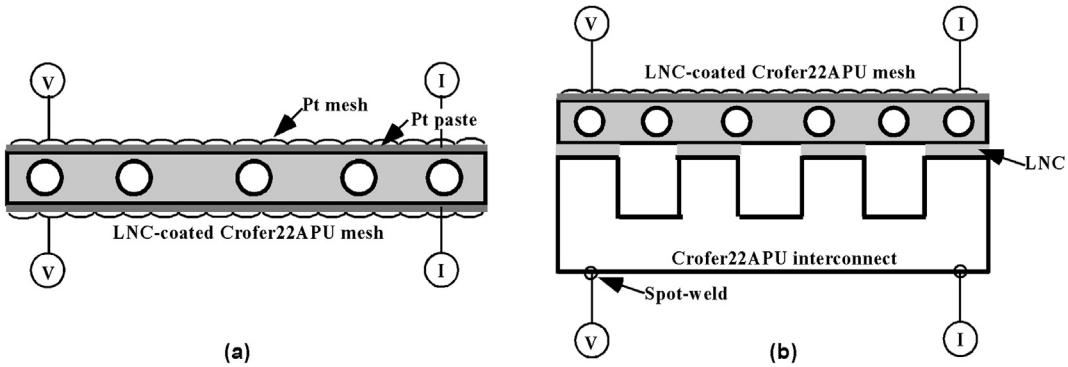

Fig. 2. Schematic view of the system configuration for ASR measurements for: a) composite contact material and b) composite contact material on channeled interconnect.

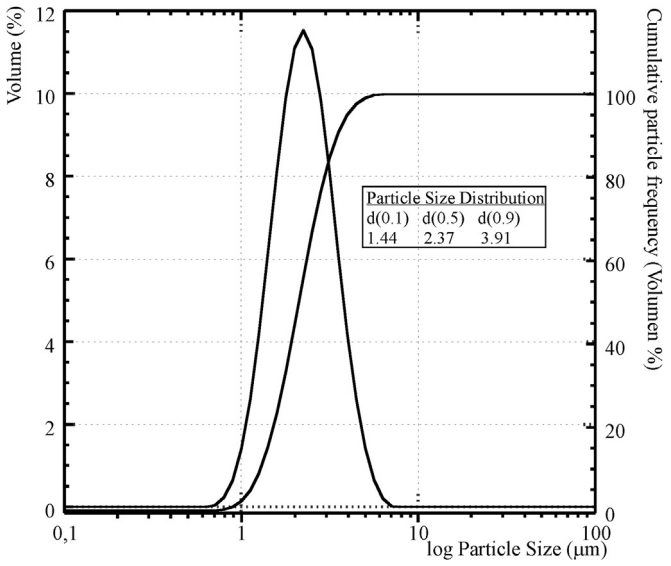

Fig. 3. Particle size distribution of LNC powder.

3.2.1. Long term stability of composite contact material

In order to study the chemical compatibility and also to establish the adherence between the ceramic and metallic parts, the sintered at 1050 °C composite contact material was heated at 800 °C for 1000 h, in open air. EDX mapping (Figs. 6 and 7) were performed of a cross-section of the composite material after long-term operation was performed, and compared with another sample just sintering at 1050 °C for 2 h used to establish initial reactivity. According to Fig. 6, the initial material showed a Cr_2O_3 and $(Mn,Cr)_3O_4$ spinel protection layer to minimize Cr migration through ceramic coated, as expected. Nevertheless, the formed passive chromia layer is not enough to prevent the migration of Cr since the evaporation of protective chromia layer takes place. Early investigations [33] revealed that $(Mn,Cr)_3O_4$ spinel offers lower volatility of Cr than chromia. However, this reduction is less than an order of magnitude. Thus, a Cr deposit ring along the edge of the LNC ceramic coated, whose width was ~35 μm, was also observed. The redeposition of chromium at the contact material, usually as poor conductive phases, could decrease the cell performance [34].

The direct contact between the ceramic contact material and the alloy makes possible solid phase diffusion of Cr [35]. However, the microstructure of the ceramic material revealed open porosity in the initial material and composite after heating at 800 °C for 1000 h in open air, allowing vapor phase transport of volatile Cr-species (CrO_3 (g), $CrO_2(OH)_2$ (g)) throughout the LNC coating. It has been found that [36] the most dominant chromium species are CrO_3 in dry air and $CrO_2(OH)_2$ in humidified air. However, the partial pressure of $CrO_2(OH)_2$ and CrO_3 varies significantly with the temperature. At the temperature decreases, $CrO_2(OH)_2$ species become increasingly dominant. The partial pressure of CrO_3 decreases rapidly with the decrease of temperature while the change in the partial pressure of $CrO_2(OH)_2$ with the temperature is relatively small. So, when the samples are sintered at 1050 °C, considering a wet atmosphere, the main chromium vapor specie is $CrO_2(OH)_2$. Besides, it could be found CrO_3 because its partial pressure is still high. However, when the samples are treated at 800 °C, the partial pressure of CrO_3 is low being the dominant specie chromium oxyhydroxide. The deposition process of these Cr species at the contact material can be described by the nucleation reaction between the high valence Cr phases and the nucleation agents (Ni^{2+},

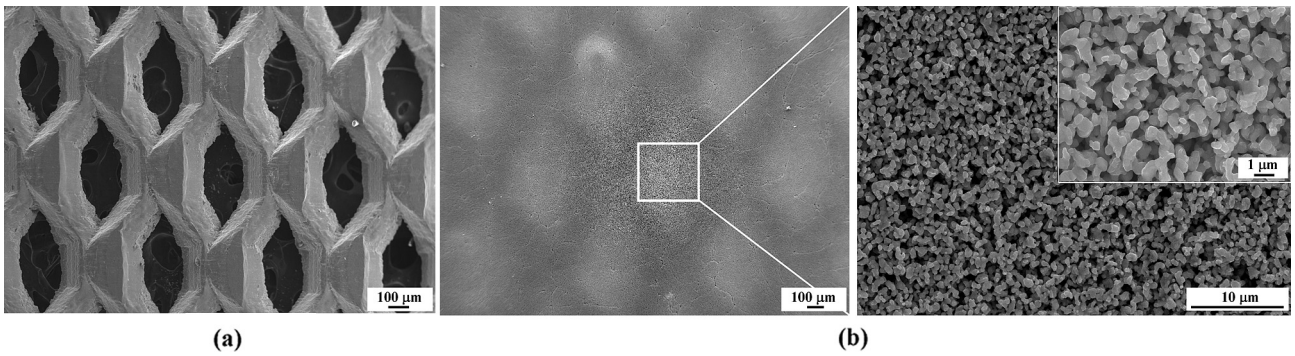

Fig. 4. Surface SEM micrographs of Fe–Cr mesh: a) before and b) after sintered LNC.

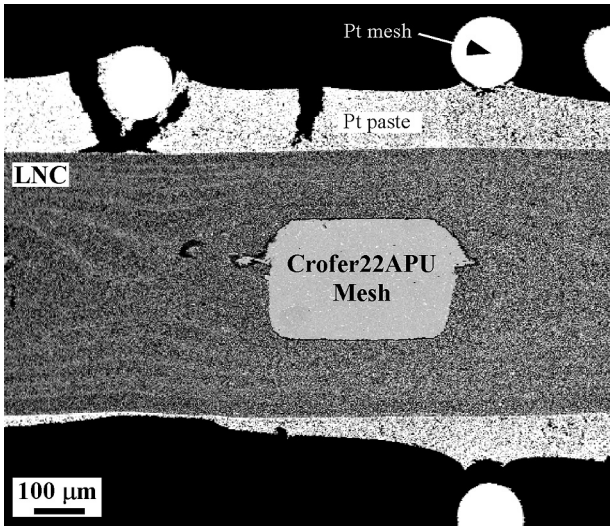

Fig. 5. SEM cross-section of the ceramic/metallic composite contact material after ASR measurements.

Co^{2+}), forming Cr–Ni^{2+}, Co^{2+}-O nucleus. The reaction between these nucleus, gaseous Cr compounds and nucleation agents leads to the deposition and formation of Cr_2O_3, $(Cr,Mn)_3O_4$, $CoCr_2O_4$, etc [3]. One should consider that [37] the magnitude of the Cr deposition is smaller with reducing the test temperature, using the same time exposure in each experiment. Thus, in first sintering step at 1050 °C the Cr deposition is accelerated by temperature and, in the long heat treatment at 800 °C by the exposure time. Thus, different ceramic material densifications were observed between the initial material and composite after the long term treatment, showing that the latter was denser. The formation of dense new phases like spinels might change the pore distribution of the ceramic material. Therefore, the microstructure of the ceramic coating depends on the reactions undergone by the material.

High magnification cross-sectional BSE micrographs and the corresponding EDX elemental line scans of the initial (Fig. 8a) and treated (Fig. 8b) material are shown in Fig. 8. According to other studies [38,39], the oxide scale growth rate is strongly affected by the temperature. With increasing temperature the growth rate constant increases exponentially. Besides, it was found [40] the chromium oxide scale rates at longer exposure time, on the cathode side, can be interpreted as being parabolic. Thus, the oxide scale formed on the mesh after 1000 h was slightly more noticeable. According to Ref. [41] and taking into account the Fe–Cr phase diagram [42], the oxide scale formed on mesh steel surface, after the sintering process of the composite at 1050 °C, is formed by FCC-Fe/Cr_2O_3 in contact with the stainless steel and, by Fe_2O_3 as the oxide surface. Between these two layers, several oxides may form, such as, Fe_3O_4, FeO, $(Cr,B)_3O_4$ spinel (B = Co, Fe, Mn, Ni) [43–45]. The similar ionic radii of Co, Fe, Mn and/or Ni, make it difficult to determine the exact chemistry of the grown spinel. At 800 °C the composition of the oxide scale has a similar trend to that at 1050 °C. However, in the oxide/metal interface Cr_2O_3 may form instead of FCC-Fe/Cr_2O_3 as in the 1050 °C case. These results are in good agreement with performed EDX line scans (Fig. 8a and b). The formation of iron oxides in oxide scale makes alloy be more susceptible to breakaway oxidation [46]. The white zones observed on alloys (Fig. 8) were identified as LNC contamination due to the polishing process. Besides, locally internal precipitates of Cr_2O_3 followed by $(Mn,Cr)_3O_4$ spinel were also found (Fig. 7). These internal precipitates could be related to the external oxide scale or it could be that the diffusion rate of oxygen in the alloy was stronger than that of Cr, forming internal Cr_2O_3 precipitates [47].

3.3. Characterization of composite contact material with channeled Crofer22APU interconnect

As starting point, the metallic substrates were oxidized at 800 °C for 100 h. This preoxidation of the steel may reduce Cr and Fe transport into the contact coating after long oxidation times [48]. A composite contact material without sintering was directly adhered

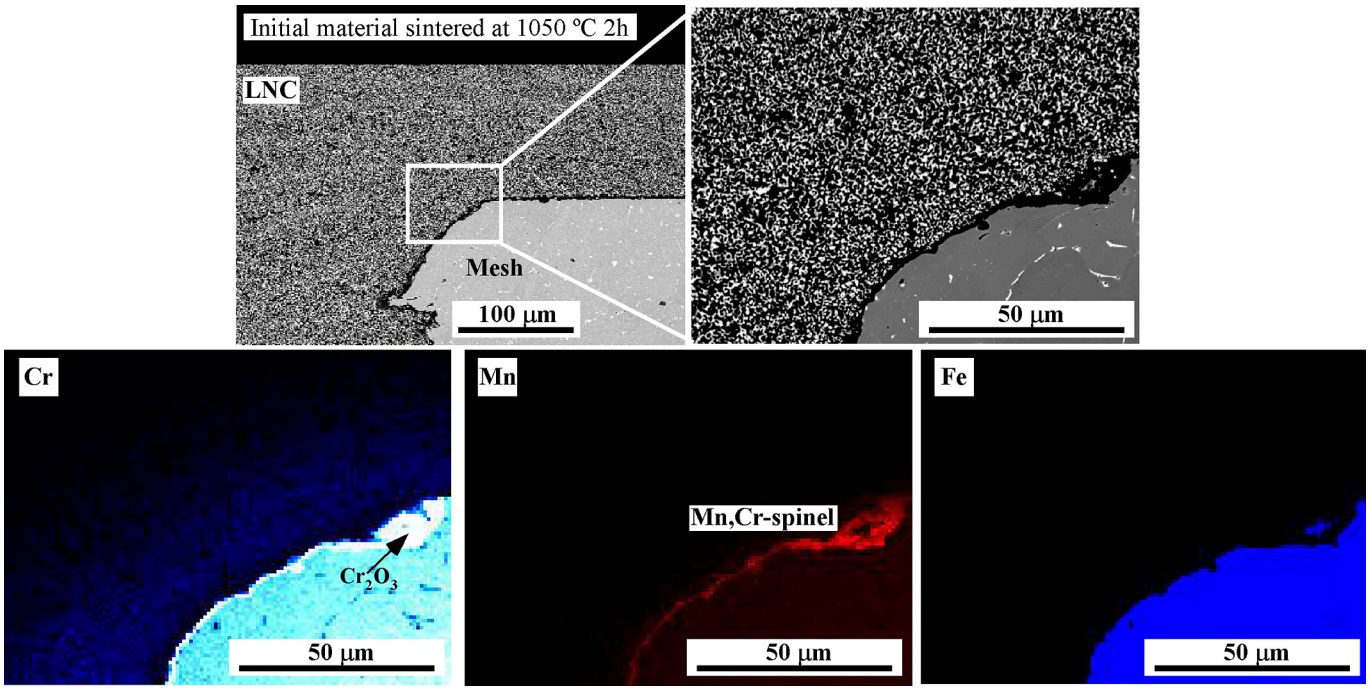

Fig. 6. Cross-section of composite contact material after sintering at 1050 °C for 2 h in air and EDX mapping of the selected zone (in white continuous line).

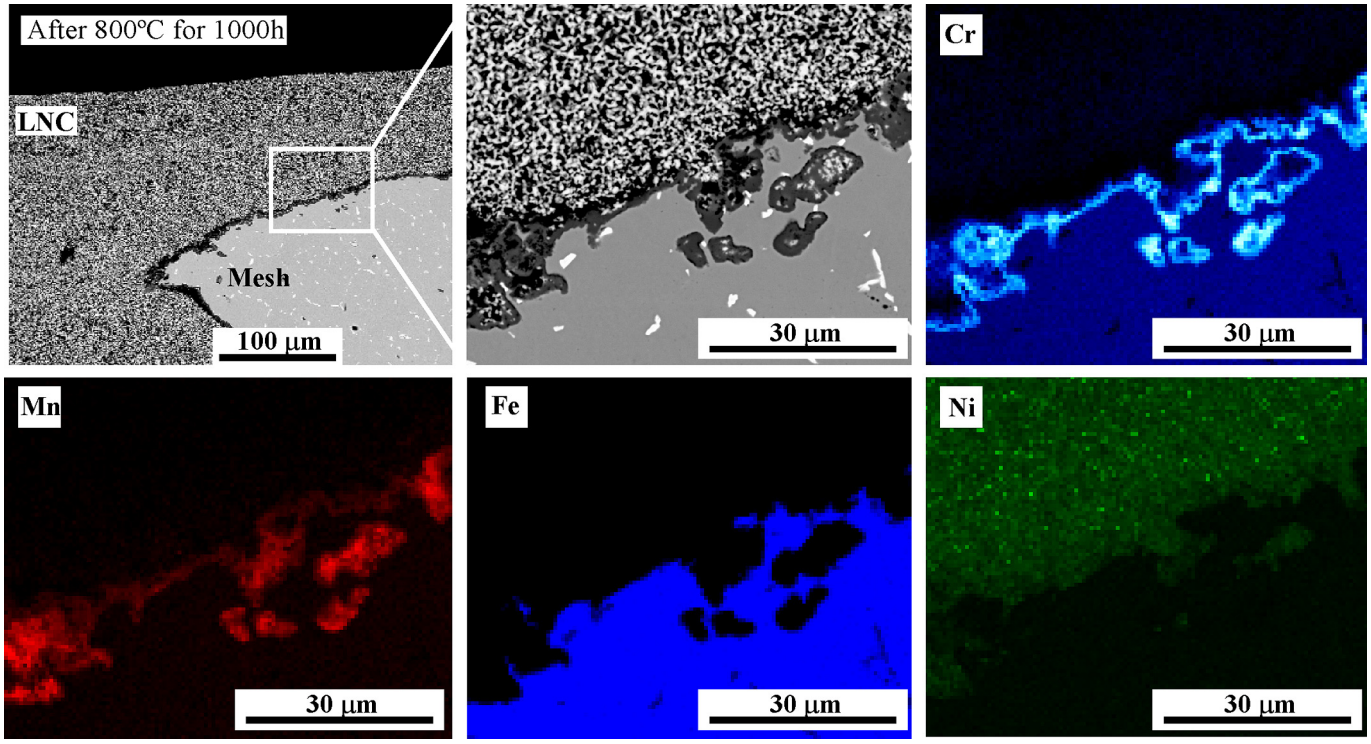

Fig. 7. Cross-section of composite contact material after heating at 800 °C for 1000 h in air and EDX mapping of the selected zone (in white continuous line).

to preoxidized channeled Crofer22APU interconnect. In order to achieve good adhesion between both materials, the ribs of the interconnect substrate were coated with LNC ceramic material by colloidal spray. Then, the system composed of {composite contact material/channeled interconnect} was sintered at 1050 °C for 2 h in open air. In order to check the reproducibility of the process, different systems were prepared. Fig. 9 and Table 3 show ASR values of two systems, indicating good stability and similar signal during the contact resistance measurements, and thus a good adherence between the composite contact material and the

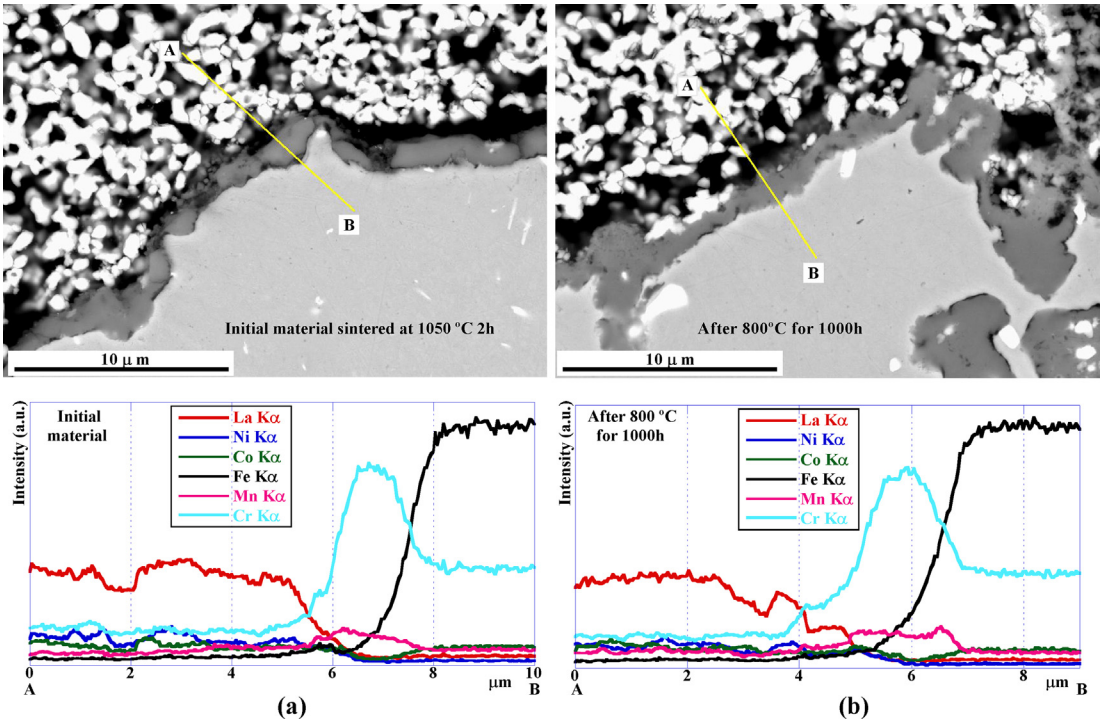

Fig. 8. Cross-sectional BSE images and the corresponding EDX elemental line scans of a) initial material and b) composite after the long heat treatment.

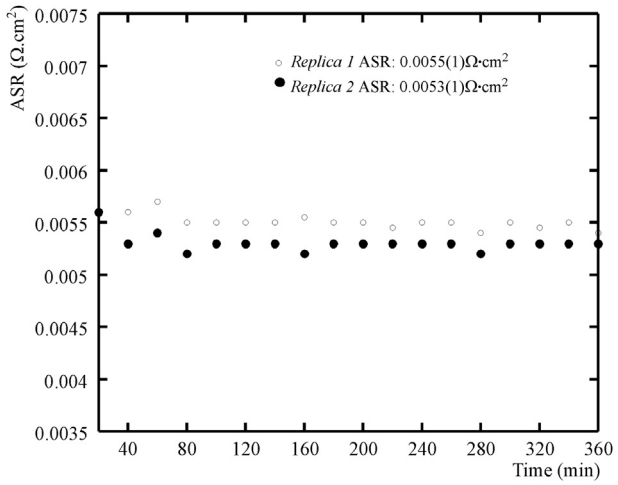

Fig. 9. ASR for {composite contact material/channeled interconnect} interface as a function of time.

Table 3
Area specific resistance values for composite contact material, with and without interconnect, measured at 800 °C in air.

Sample	≈ASR (mΩ cm^2)
Composite contact material	0.46 ± 0.01
Replica 1	5.50 ± 0.01
Replica 2	5.30 ± 0.01

interconnect. The ASR values are in good agreement with those obtained in {Crofer22APU interconnect without channels/LNC contact layer/$La_{0.6}Sr_{0.4}FeO_3$ cathode} system [17]. The contact composite/interconnect ASR value was 5.40 ± 0.01 mΩ cm^2, which is a suitable value for the performance of IT-SOFC stack. In addition, the obtained ASR value is lower than the systems without applying a contact layer [12,16,17]. According to SEM cross-section of the system after ASR measurements with EDX mapping to estimate element diffusion (Fig. 10), the formed oxide scale acts as protective layer: Cr_2O_3 followed by $(Cr,Mn)_3O_4$ spinel top layer. The composite direct contacted (the rib) and indirect contacted (channel) with the interconnect present similar Cr, Mn and Fe distributions. Along the ceramic bulk, Cr^{3+} and Mn^{2+} deposition was observed, indicating that Mn dopant promotes Cr deposition on the ceramic material.

3.3.1. *Long term stability of composite contact material with channeled Crofer22APU interconnect*

The {LNC dip-coated on Crofer22APU mesh composite contact material/Crofer22APU channeled interconnect} sintered system at 1050 °C, was treated at 800 °C for 1000 h in open air to study the long term compatibility between the metallic substrate and the composite. Fig. 11 shows X-ray Micro-Diffraction pattern refinements performed on the rib (right) and the channel (left) of the interconnect in contact with the composite material, after the long term treatment. The preliminary analysis of the studied points was carried out using the X'Pert HighScore software 2003. After the identification, the observed phases, in both areas, were quantified; full-profile refinements were performed using the FULLPROF program [49]. The formed phases and their semiquantitative analysis (% in weight) are presented in Table 4. These analyses reveal that in the rib zone the main phases were $LaNi_{0.6}Co_{0.4}O_{3-\delta}$, La(Cr, B)$O_3$ (B = Ni, Co) and NiO. In addition, secondary phases were also detected: Fe–Cr, $(Cr,B)_3O_4$ spinel (B = Co, Fe, Mn, Ni) and Fe_2O_3. In contrast, the channel zone present as main phases $LaNi_{0.6}Co_{0.4}O_{3-\delta}$, Fe_3O_4, La(Cr, B)O_3 (B = Ni, Co), Cr_2O_3 and as secondary phases: Fe–Cr, $(Cr, B)_3O_4$ (B = Co, Fe, Mn, Ni) spinel and Fe_2O_3. The original Fe–Cr substrate was identified indicating that the X-ray penetration was enough to observe the signal of all the formed layers. The quality factors of the refinements are given in Tables 5 and 6. The presence of the LNC perovskite phase in the channel zone is probably due to the contamination during the spray deposition on the ribs. The presence of NiO might entail that Ni is partially

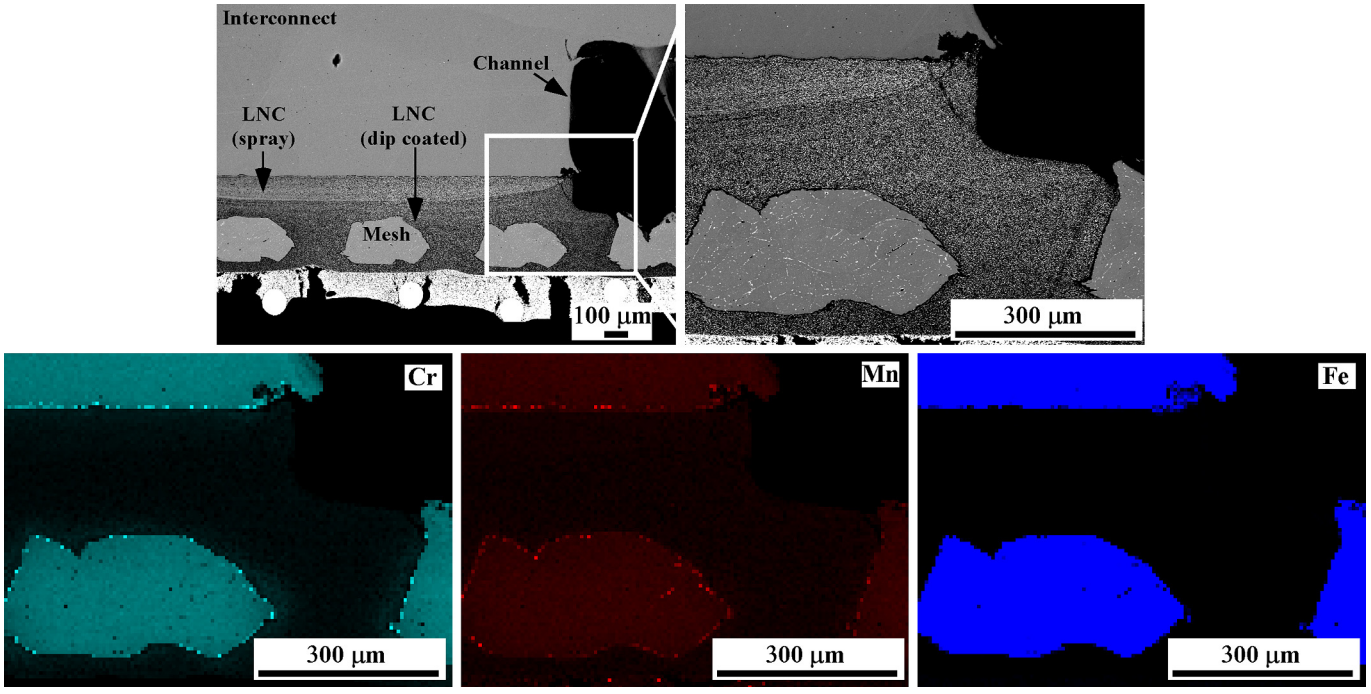

Fig. 10. Cross-section of {composite contact material/channeled interconnect} sintered system after ASR test and EDX mapping of the selected zone (in white continuous line).

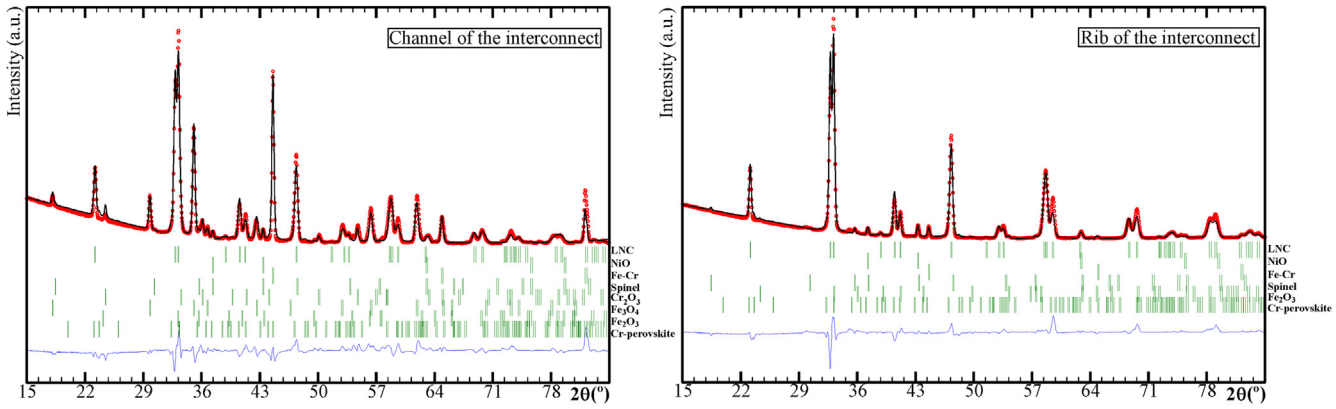

Fig. 11. X-ray Micro-Diffraction pattern refinements performed on the rib and on channel of the interconnect in contact with composite material, after long term heat treatment.

extracted from the LNC perovskite lattice, whereas Cr is incorporated, most likely to form La(Ni, Co, Cr)O_3 [27,50]. It is known that applying a protective layer to the metallic interconnect alloy can reduce the oxidation rate [34]. Fig. 12 shows cross-section EDX elemental line scans performed on the channel (Fig. 12a) and on the rib (Fig. 12b) of the interconnect, which was in contact with the composite material after treated at 800 °C for 1000 h in open air. The surface oxide layers, both on the channel and on the rib, of the interconnect range from approximately 0.5 to 2 μm. Before ASR test, the metallic substrate was preoxidized at 800 °C for 100 h, making difficult to observe differences between both zones. However, the Fe and Cr detected in the channel is bigger than in the rib, probably due to the formation of a passive layer on the metal surface, more severe in the case of an uncoated area. According to this, ceramic coating might act as a protective layer. Hence, Cr_2O_3 is observed on the channels. Furthermore, the absence of Cr_2O_3 on the rib of the interconnect, can also imply that it has completely reacted to form La(Cr, B)O_3 (B = Ni, Co) and (Cr, B)$_3O_4$ (B = Mn, Fe, Ni, Co) phases. The formed oxides at analyzed channel zones contain: Fe_2O_3 (<2% in weight) and Fe_3O_4 (~36% in weight) whereas for those on the rib zone, Fe_2O_3 (~2% in weight) was semi-quantified. The presence of iron oxides is in good agreement with the previous studies performed on composite contact material (Section 3.2.1.). According to XRMD results, an interconnect without ceramic coating at long exposure rate to air, can promote the Fe_3O_4 formation rather than the formation of a chromia/spinel protective scale, concluding in the formation of non-protective or Fe-rich scale.

Fig. 13 shows the surface of the composite material which was in contact with the interconnect, after long term IT-SOFC conditions. EDX mapping analysis is also shown. Three different areas were identified at the composite contact surface: the area of the composite i) under the rib and, ii) under channel of the interconnect and, iii) the interface between both zones. Formation of Cr and Mn deposit along the interface of both areas is observed, probably in the form of (Cr,Mn)$_3O_4$ protective spinel. Besides, EDX analysis showed that the zone under the channel presents Cr, Mn and La enrichment, possibly associated with Cr–Mn-spinel and Cr-perovskite crystalline phases. The significant difference in the amount of Cr deposition on the composite material surface under the rib and under the channel of the interconnect can indicate that the direct exposure to air accelerates the formation of CrO_3 (g) and $CrO_2(OH)_2$ (g) species. Thus, vapor phase transport of Cr specie molecules would be much faster and more significant than the solid phase diffusion of atoms, in LNC and chromia scale, through defects in these solids. Increasing volatile Cr species enhances Cr-depletion from the alloy, thereby enabling the formation of iron oxides [46].

XPS measurements were performed on the observed channel and rib contact areas of the surface of the metallic/ceramic composite material. Fig. 14 shows high resolution spectra of the different zones including La $3d_{5/2}$, Cr 2p and Mn $2p_{3/2}$ spectral regions. The binding energies and relative atomic percentage concentration of the detected elements are listed in Tables 7 and 8, respectively. In both studied areas, for La, there are two peaks, one at 833 eV which corresponds to La^{3+} in perovskite phase [51] and, another at 834 eV which is assigned to La^{3+} in La_2O_3 [52]. In addition, the peaks appearing at 575 eV and 579 eV could be assigned to Cr^{3+} in perovskite [53,54]. The atomic concentration of Cr assigned to the perovskite remains a ratio of 1:1, and La component is assigned to the binding energy of 833 eV, in good agreement with ABO_3 structure (Tables 6 and 7). In the contact channel zone, the peak at 577 eV might be ascribed to Cr^{3+} species,

Table 4
Semiquantitative % in weight of the formed phases on the rib and channel of the interconnect in contact with composite material after heating at 800 °C for 1000 h.

Phases (space group)	N° PDF	Channel	Rib
$LaNi_{0.6}Co_{0.4}O_3$ (R-3c)	32-0296	~46	~82
$LaCrO_3$ (Pbnm)	24-1016	~6	~7
Fe–Cr (Im3m)	34-0396	<2	<2
Fe_2O_3 (R-3c)	73-2234	<2	~2
NiO (Fm-3m)	73-1519	~2	~5
$MnCr_2O_4$ (Fd-3m)	31-630	<2	<2
Cr_2O_3 (R-3c)	85-0730	~4	–
Fe_3O_4 (Fd-3m)	19-629	~36	–

*Estimated error: ± 1–2%.

Table 5
The quality of refinement performed on the rib of the interconnect in contact with composite material, after long term heat treatment.

Rib phases	$LaNi_{0.6}Co_{0.4}O_3$	$LaCrO_3$	Fe–Cr	Fe_2O_3	NiO	$MnCr_2O_4$
R_{Bragg}	13	29	31	30	16	40
R_f	8	23	16	24	9	18
χ^2	5					

Table 6
The quality of refinement performed on the channel of the interconnect in contact with composite material, after heated at 800 °C for 1000 h.

Channel phases	$LaNi_{0.6}Co_{0.4}O_3$	$LaCrO_3$	Fe–Cr	Fe_2O_3	NiO	$MnCr_2O_4$	Cr_2O_3	Fe_3O_4
R_{Bragg}	13	32	21	43	13	32	31	18
R_f	10	25	11	29	11	21	18	11
χ^2	18							

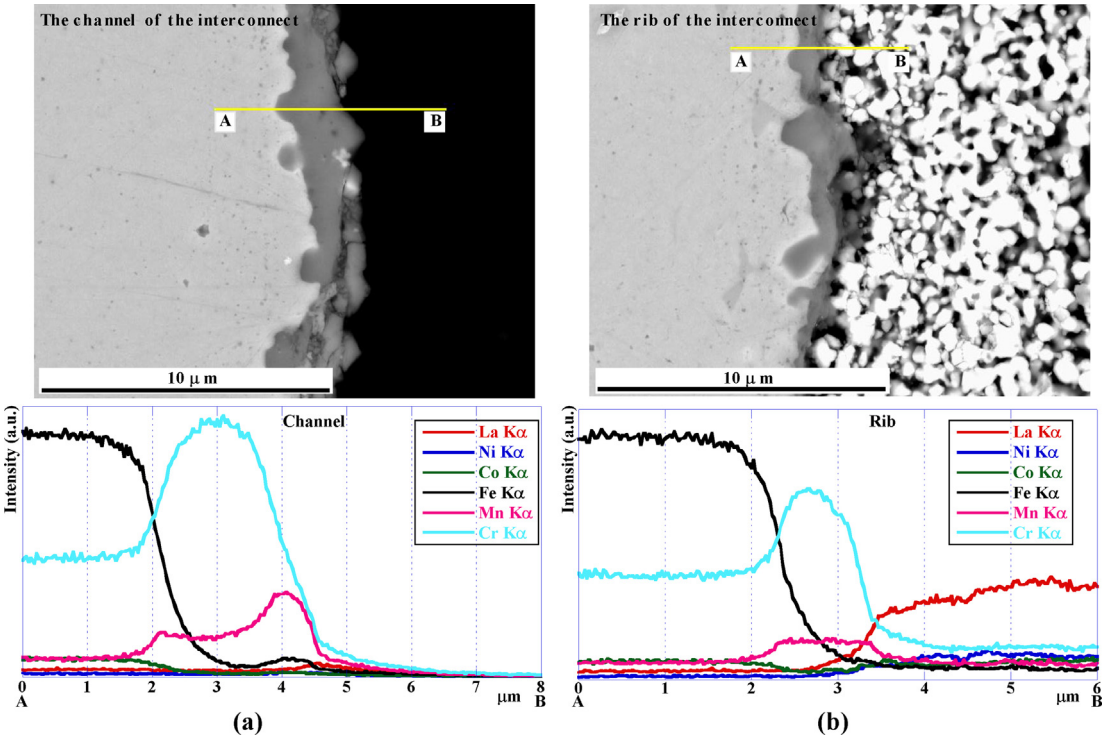

Fig. 12. Cross-sectional BSE images and the corresponding EDX elemental line scans performed on a) the channel and b) the rib of the interconnect which was in contact with the composite contact material after treated at 800 °C for 1000 h in open air.

possibly forming Cr_2O_3 [55] in good agreement with XRD results. The binding energy of 642 eV, which corresponds to Mn $2p_{3/2}$, is in good agreement with Mn^{4+} in MnO_2 superficial oxide [56]. However, the content of Mn is too low to be assigned to Mn^{2+} or Mn^{4+} species.

4. Conclusions

The application of composite LNC/Crofer22APU mesh coatings as a contact material for Fe–Cr channeled interconnect was studied as a solution to limit electrical losses between both materials and

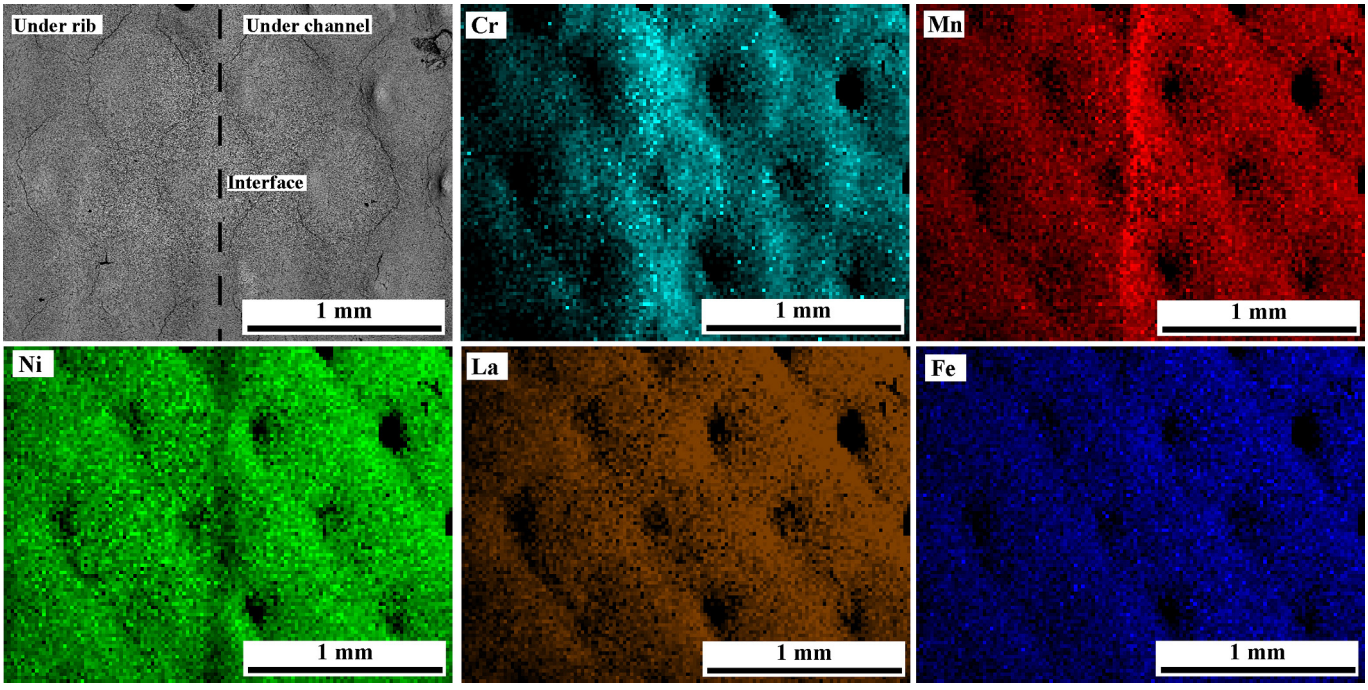

Fig. 13. EDX mapping of the surface of the composite material which was in contact with interconnect, after long term IT-SOFC conditions.

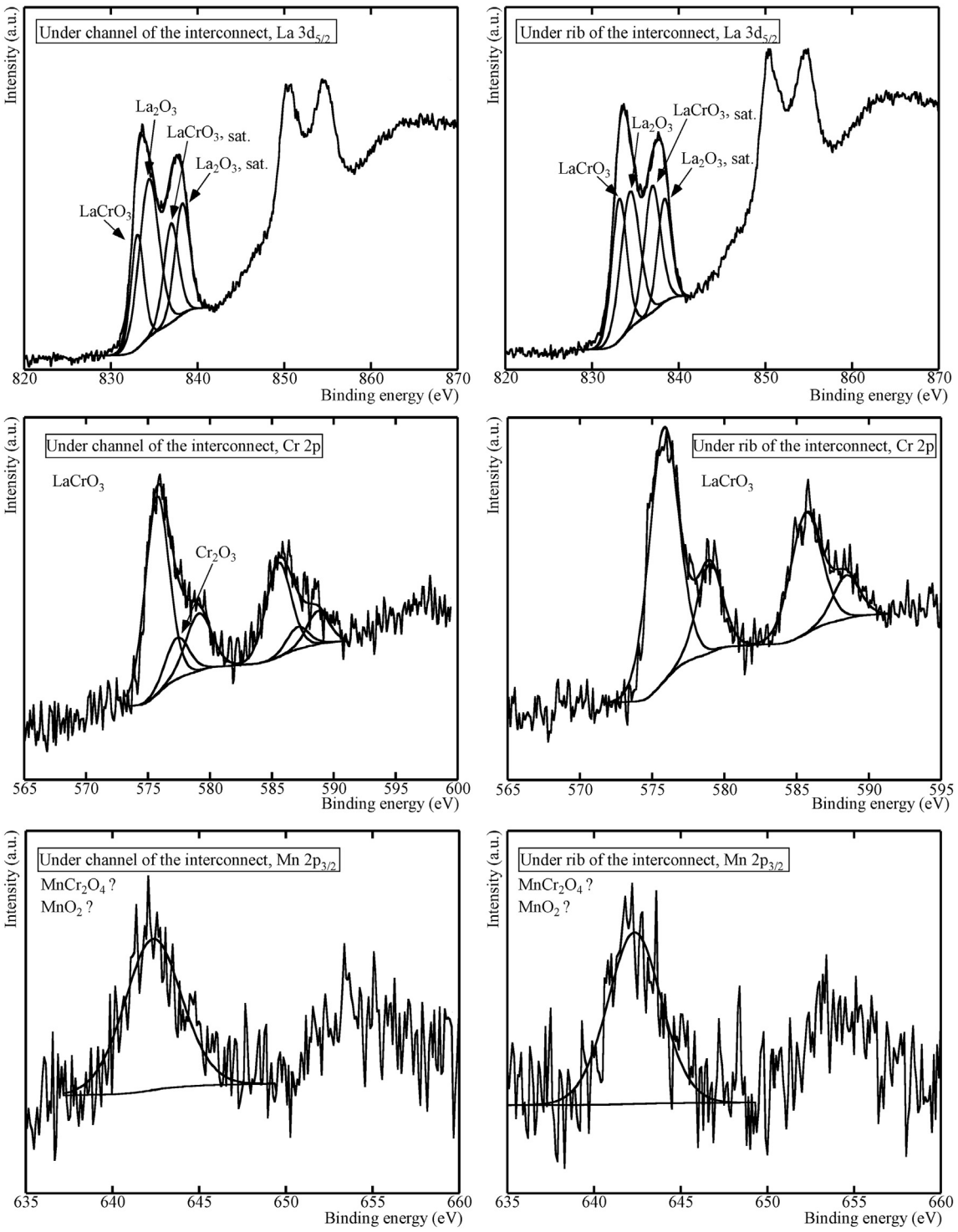

Fig. 14. La $3d_{5/2}$, Cr 2p and Mn $2p_{3/2}$ spectral regions of the surface of composite contact material under the rib and channel after long term heated at 800 °C in air.

also to reduce chromium migration from the interconnect. Prior to forming the composite material, adequate formulation of the LNC paste was obtained and characterizated by rheological measurements. This slurry was dip coated on Fe–Cr mesh to obtain metallic-ceramic composite contact material. The results showed good adherence between ceramic and metallic material, showing a continuous and homogeneous coated LNC layer. The system presented an ASR value of 0.46 ± 0.01 mΩ cm^2 at 800 °C. After treatment under long term IT-SOFC conditions, the composite material still present noticeable oxide scale and adequate mechanical integrity of the LNC/Fe–Cr mesh interface.

When the composite contact material was directly adhered to the interconnect, the obtained ASR values were reproducible and stable indicating good adherence between the composite material and interconnect. After 1000 h at 800 °C in open air, X-ray Micro-Diffraction, performed at the rib and channel of the interconnect,

Table 7
XPS analysis results of the detected elements for the contact surface of the composite in contact with the rib of the interconnect, after heating at 800 °C for 1000 h in air.

Peak	Binging energy (eV)	% at. Conc.
La $3d_{5/2}$ in ABO_3	833.14	9.5
La $3d_{5/2}$ in La_2O_3	834.4	9.1
Cr 2p in ABO_3	575.82; 578.98	9.1
Mn $2p_{3/2}$	642.35	3.2
O 1s	528.93; 530.74	69.1

Table 8
XPS analysis results of the detected elements for the contact surface of the composite under channel of the interconnect, after heating at 800 °C for 1000 h in air.

Peak	Binging energy (eV)	% at. Conc.
La $3d_{5/2}$ in ABO_3	833.07	7.1
La $3d_{5/2}$ in La_2O_3	834.41	11.8
Cr 2p in ABO_3	575.73; 579.1	7.2
Cr 2p in Cr_2O_3	577.35	1.1
Mn $2p_{3/2}$	642.34	3.2
O 1s	528.98; 530.99	69.6

revealed interactions between the oxide scale and the LNC material to form Cr-perovskite which was related with NiO presence. In both zones semi-quantified Fe_2O_3 was also present, arising from the oxidation of the metal itself. According to XRMD results, the interconnect without ceramic coating on the metal surface, and the direct exposure to air increased the oxidation rate and Fe_3O_4 formation as non-protective layer. The direct exposure to air accelerates the formation of CrO_3 (g) and $CrO_2(OH)_2$ (g) species on channel surface.

Taking into account the obtained contact resistance, mechanical integrity and chemical compatibility of the studied system, LNC dip-coated on Fe–Cr mesh would offer promising opportunities as a high conductivity composite contact material. Future work will include the integration of the $La_{0.6}Sr_{0.4}FeO_3$ cathode to form {interconnect/composite contact material/cathode} system, in flow channel configuration, to study its long-term stability in terms of contact resistance and chemical compatibility.

Acknowledgment

This research has been funded by the Dpto. Educación, Política Lingüística y Cultura of the Basque Goverment (IT-630-13), Ministerio de Ciencia e Innovación (MAT2010-15375 and MAT2012-30763) and Engineering and Physical Sciences Research Council (EP/I003932). The authors thank SGIker technical support and Dr. Mª Belén Sánchez Martínez de Ilárduya for XPS measurements. A. Morán-Ruiz thanks UPV/EHU for funding her PhD work.

References

[1] J. Klugman, Human Development Report 201. Sustainability and Equity: a Better Future for All, United Nations Development Programme, New York, USA, 2011.
[2] B.J. Spivey, T.F. Edgar, J. Process Contr. 22 (2012) 1502.
[3] S.P. Jiang, X. Chen, Int. J. Hydrogen Energy 39 (2014) 505.
[4] K. Huang, S.C. Singhal, J. Power Sources 237 (2013) 84.
[5] S.C. Singhal, Solid State Ionics 135 (2000) 305.
[6] J. Wu, X. Liu, J. Mater. Sci. Technol. 26 (4) (2010) 293.
[7] C. Sun, R. Hui, J. Roller, J. Solid State Electrochem. 14 (2010) 1125.
[8] A. Mat, B. Timurkutluk, C. Timurkutluk, Y. Kaplan, Ceram. Int. (2014), http://dx.doi.org/10.1016/j.ceramint.2014.01.073.
[9] W.B. Guan, H.J. Zhai, L. Jin, T.S. Li, W.G. Wang, Fuel Cells 3 (2011) 445.
[10] W. Wu, G.L. Wang, W.B. Guan, Y.F. Zhen, W.G. Wang, Fuel Cells 5 (2013) 743.
[11] W. Guan, L. Jin, W. Wu, Y. Zheng, G. Wang, W.G. Wang, J. Power Sources 245 (2014) 119.
[12] X. Montero, F. Tietz, D. Stöver, M. Cassir, I. Villarreal, J. Power Sources 188 (2009) 148.
[13] L. Jin, W. Guan, J. Niu, X. Ma, W.G. Wang, J. Power Sources 240 (2013) 796.
[14] W. Zhang, F. Wang, K. Wang, J. Pu, B. Chi, L. Jian, Int. J. Hydrogen Energy 37 (2012) 17253.
[15] F. Wang, D. Yan, W. Zhang, B. Chi, J. Pu, L. Jian, Int. J. Hydrogen Energy 38 (2013) 646.
[16] Z. Yang, G. Xia, P. Singh, J.W. Stevenson, J. Power Sources 155 (2006) 246.
[17] A. Morán-Ruiz, K. Vidal, M.A. Laguna-Bercero, A. Larrañaga, M.I. Arriortua, J. Power Sources 248 (2014) 1067.
[18] M.C. Tucker, L. Cheng, L.C. DeJonghe, J. Power Sources 196 (2011) 8313.
[19] M.C. Tucker, L. Cheng, L.C. DeJonghe, J. Power Sources 196 (2011) 8435.
[20] M.C. Tucker, L. Cheng, L.C. DeJonghe, J. Power Sources 224 (2013) 174.
[21] Z. Lu, G. Xia, J.D. Templeton, X. Li, Z. Nie, Z. Yang, J.W. Stevenson, Electrochem. Commun. 13 (2011) 642.
[22] Q.X. Fu, D. Sebold, F. Tietz, H.P. Buchkremer, Solid State Ionics 192 (2011) 376.
[23] N. Shaigan, D.G. Ivey, W. Chen, J. Power Sources 185 (2008) 331.
[24] L.T. Wilkinson, J.H. Zhu, J. Electrochem. Soc. 156 (8) (2009) B905.
[25] X. Montero, N. Jordán, J. Pirón-Abellán, F. Tietz, D. Stöver, M. Cassir, I. Villarreal, J. Electrochem. Soc. 156 (1) (2009) B188.
[26] V. Miguel-Perez, A. Martínez-Amesti, M.L. Nó, A. Larrañaga, M.I. Arriortua, Corros. Sci. 60 (2012) 38.
[27] A. Morán-Ruiz, K. Vidal, A. Larrañaga, M.I. Arriortua, Fuel Cells 3 (2013) 398.
[28] A. Torabi, T.H. Etsell, P. Sarkar, Solid State Ionics 192 (2011) 372.
[29] L. Conceicao, L. Dessemond, E. Djurado, M.M.V.M. Souza, Int. J. Hydrogen Energy 38 (2013) 15335.
[30] K. Hilpert, D. Das, M. Miller, D.H. Peck, R. Wei, J. Electrochem. Soc. 143 (1996) 3642.
[31] V. Miguel Pérez, Interconectores Metálicos y Capas Protectoras para su Aplicación en pilas SOFC, UPV/EHU, 2013. Ph. D. thesis.
[32] D.K. Schroder, Semiconductor Material and Device Characterization, third ed., John Wiley & Sons, New York, 1998, pp. 149–156. Cap. 3.
[33] J.P. Choi, K.S. Weil, Y.M. Chou, J.W. Stevenson, Z.G. Yang, Int. J. Hydrogen Energy 36 (2011) 4549.
[34] V. Miguel-Pérez, A. Martínez-Amesti, M.L. Nó, A. Larrañaga, M.I. Arriortua, J. Power Sources 243 (2013) 419.
[35] G.Y. Lau, M.C. Tucker, C.P. Jacobson, S.J. Visco, S.H. Gleixner, L.C. DeJonghe, J. Power Sources 195 (2010) 7540.
[36] X. Chen, Y. Zhen, J. Li, S.P. Jiang, Int. J. Hydrogen Energy 35 (2010) 2477.
[37] S.P. Jiang, S. Zhang, Y.D. Zhen, J. Mater. Res. 20 (3) (2005) 747.
[38] P. Kofstad, High Temperature Corrosion, Springer, 1988.
[39] M. Palcut, L. Mikkelsen, K. Neufeld, M. Chen, R. Knibbe, P.V. Hendriksen, Corros. Sci. 52 (2010) 3309.
[40] M. Linder, T. Hocker, L. Holzer, K.A. Friedrich, B. Iwanschitz, A. Mai, J.A. Schuler, J. Power Sources 243 (2013) 508.
[41] V.S. Dheeradhada, H. Cao, M.J. Alinger, J. Power Sources 196 (2011) 1975.
[42] J.O. Anderson, B. Sundman, Calphad 11 (1987) 83.
[43] K. Wang, Y. Liu, J.W. Fergus, J. Am. Ceram. Soc. 94 (12) (2011) 4490.
[44] W.J. Shong, C.K. Liu, C.Y. Chen, C.C. Peng, H.J. Tu, G.T.K. Fey, R.Y. Lee, H.M. Kao, Mater. Chem. Phys. 127 (2011) 45.
[45] K. Przybylski, T. Brylewski, E. Durda, R. Gawel, A. Kruk, J. Therm. Anal. Calorim. doi: 10.10007/s10973-013-3594-1.
[46] E. Essuman, G.H. Meier, J. Zurek, M. Hänsel, T. Norby, L. Singheiser, W.J. Quadakkers, Corros. Sci. 50 (2008) 1753.
[47] H. Ali-Löytty, Microalloying Mediated Segregation and Interfacial Oxidation of FeCr Alloys for Solid-oxide Fuel Cell Applications, Tampereen teknillinen yliopisto – Tampere University of Technology, 2013. Ph. D. thesis.
[48] K.O. Hoyt, P.E. Gannon, P. White, R. Tortop, B.J. Ellingwood, H. Khoshuei, Int. J. Hydrogen Energy 37 (2012) 518.
[49] J. Rodríguez-Carvajal, Fullprof Rietveld Pattern Matching Analysis of Power Patterns, 1994. Grenoble.
[50] M.K. Stodolny, B.A. Boukamp, D.H.A. Blank, F.P.F. van Berkela, J. Electrochem. Soc. 158 (2) (2011) B112.
[51] F. Bin, C. Song, G. Lv, J. Song, C. Gong, Q. Huang, Ind. Eng. Chem. Res. 50 (2011) 6660.
[52] C.D. Wagner, W.M. Riggs, L.E. Davis, J.F. Moulder, G.E. Mullenberg, Handbook of X-ray Photoelectron Spectroscopy, Perkin-Elemer Corporation, Physical Electronics Division, Eden Prairie, MN 55344, 1979.
[53] W.Y. Howng, R.J. Thorn, J. Chem. Phys. Solids 41 (1980) 75.
[54] M. Stojanovic, R.G. Haverkamp, C.A. Mims, H. Moudallal, A.J. Jacobson, J. Catal. 165 (1997) 315.
[55] C. Battistoni, J.L. Dormann, D. Fiorani, E. Paparazzo, S. Viticoli, Solid State Commun. 39 (1981) 581.
[56] A. Aoki, Jpn. J. Appl. Phys. 15 (1976) 305.